ACSNANO
www.acsnano.org
ARTICLE

# Mechanically Tunable Dielectric Resonator Metasurfaces at Visible Frequencies

Philipp Gutruf,[†,‡,#] Chengjun Zou,[§,#] Withawat Withayachumnankul,[§,∥] Madhu Bhaskaran,[†,‡] Sharath Sriram,[†,‡] and Christophe Fumeaux*[,§]

[†]Functional Material and Microsystems Research Group and [‡]Micro Nano Research Facility, RMIT University, Melbourne, Victoria 3000, Australia

[§]School of Electrical and Electronic Engineering, The University of Adelaide, Adelaide, South Australia 5005, Australia

[∥]Interdisciplinary Graduate School of Science and Engineering, Tokyo Institute of Technology, Ookayama, Merguro-ku, Tokyo 152-8552, Japan

Supporting Information

**ABSTRACT:** **Devices that manipulate light represent the future of information processing. Flat optics and structures with subwavelength periodic features (metasurfaces) provide compact and efficient solutions. The key bottleneck is efficiency, and replacing metallic resonators with dielectric resonators has been shown to significantly enhance performance. To extend the functionalities of dielectric metasurfaces to real-world optical applications, the ability to tune their properties becomes important. In this article, we present a mechanically tunable all-dielectric metasurface. This is composed of an array of dielectric resonators embedded in an elastomeric matrix. The optical response of the structure under a uniaxial strain is analyzed by mechanical−electromagnetic co-simulations. It is experimentally demonstrated that the metasurface exhibits remarkable resonance shifts. Analysis using a Lagrangian model reveals that strain modulates the near-field mutual interaction between resonant dielectric elements. The ability to control and alter inter-resonator coupling will position dielectric metasurfaces as functional elements of reconfigurable optical devices.**

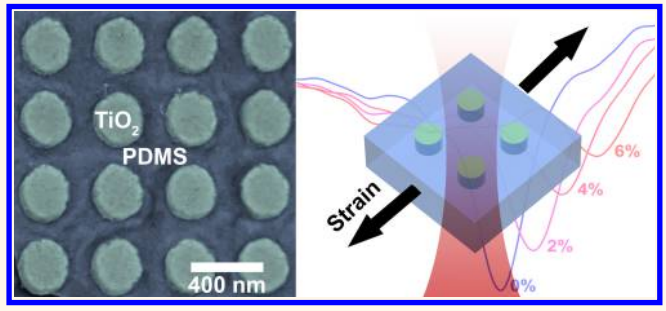


**KEYWORDS:** *nanophotonics, stretchable electronics, subwavelength structures, metasurfaces, dielectric resonators*

Next-generation optical devices require components that are compact, efficient, and reconfigurable. At visible wavelengths, conventional optical components are usually based on geometrical optics, rendering them bulky. Optical metasurfaces seek to revolutionize realization of optical components by utilizing planar thin film layers of subwavelength resonant elements.[1,2] Metasurfaces allow us to engineer phase discontinuities across the thin film interfaces.[3] This concept breaks the dependence on phase retardation arising from optical path length in bulky optics and thus allows us to realize exotic functionality, including anomalous reflection and refraction,[4,5] or broadband polarization conversion.[6] As such, metasurfaces promise unparalleled applications in sensing,[2] imaging,[7] and communications.[8]

To ensure that the functionality of metasurfaces can be harnessed for real-world applications, the ability to tune their response becomes important.[9] The inherent resonant nature of metasurfaces allows their electromagnetic responses to be tuned in many different ways. For instance, different resonance modes[10] can be tuned by changing resonators' relative orientations[11,12] or their geometries.[13] The metasurface tunability can also be achieved by manipulating the near-field interactions *via* varying unit cell periods.[14−17] Other methods to achieve tunable metasurfaces or metamaterials include the use of phase-change materials,[18,19] voltage-controlled coupling,[20] and thermal stimulus.[21] Incorporating resonant elements on stretchable substrates enables mechanical tuning of the optical responses of metasurfaces.[22−24] Additionally, in many metasurface designs, nonlinear materials have been introduced into resonant electromagnetic fields to enhance tunable higher order harmonic generation.[25,26]

Apart from the tunability, efficiency is another factor to consider for metasurfaces in real-world applications. In the past few years, a number of metasurfaces made of dielectric resonators have been demonstrated for efficient light manipulations.[6,27−31] Different from metallic resonators that intrinsically impose considerable ohmic loss in the optical regime, dielectric resonators operating *via* displacement currents can exhibit high efficiency[32] even in the visible range. An array of dielectric resonator

Received: September 22, 2015
Accepted: November 29, 2015
Published: November 30, 2015

  

DOI: 10.1021/acsnano.5b05954
*ACS Nano* 2016, 10, 133−141

nanoantennas on a metallic substrate has been experimentally demonstrated as an efficient beam deflector at visible frequencies,[27,33] and a similar structure has been proposed for implementing plasmonic couplers.[34] Also realized in the reflection mode, a uniform array of rectangular dielectric resonators on a silver substrate has been demonstrated as a broadband polarization converter.[6] It is known that high-permittivity low-loss dielectric resonators can support localized electric and magnetic resonances.[35] By spectrally and spatially overlapping both resonances,[29] a unidirectional scattering can be achieved, and thus, a highly directional radiating Huygens' surface[31] can be realized. Recently, Sautter *et al.* have demonstrated an all-dielectric metasurface made of cylindrical silicon dielectric resonators covered by a nematic liquid crystal.[36] By changing the operation temperature, the material phase of the liquid crystal and thus the near-field interactions of the resonators operating in magnetic and electric modes are altered, resulting in a demonstrated tunability of the all-dielectric metasurface.

In this article, we propose a mechanically tunable metasurface design made of an array of uniform $TiO_2$ (anatase) cylindrical dielectric resonators embedded in an elastomeric matrix. The elastomeric matrix, namely, polydimethylsiloxane (PDMS), is commonly used in stretchable technologies[22,37] as a flexible substrate due to its remarkable elasticity and low optical losses. With recent advances in stretchable electronics fabrication,[38] brittle oxides can be integrated into elastomers through a unique transfer technique allowing for high process temperatures.[39] Using this technique, a very high resolution of the embedded features can be achieved, limited only by the lithographic patterning techniques. The deformation of the soft PDMS allows for tuning the period of the array without altering the shape of the hard $TiO_2$ resonators, thus providing a convenient and viable metamaterial tuning method. Such a tuning strategy has been recently reported for tunable coloration based on high-index nonresonant diffraction grating with multimode interferences.[40] To analyze the resonant-metasurface design, mechanical and electromagnetic finite-element co-simulations have been adopted, and the results have been verified at visible frequencies with measurements performed on a fabricated prototype metasurface. To shed light on the underlying tuning mechanisms, we have analyzed the near-field interactions among dielectric resonators with a Lagrangian model[14−16] to interpret the observed resonance shifts. This work proposes an approach to achieve all-dielectric mechanically reconfigurable metasurfaces that enable the next-generation optical devices and adaptive photonic systems.

## RESULTS AND DISCUSSION

**Design and Fabrication of the Dielectric Metasurfaces.** We propose a dielectric resonator-based, mechanically tunable metasurface design operating at visible wavelengths. The tunable dielectric metasurface consists of a uniform array of cylindrical $TiO_2$ resonators embedded in an elastomeric PDMS matrix. In the considered frequency range from 450 to 600 THz, the measured average relative permittivity of $TiO_2$ is 5.8, while PDMS has an isotropic relative permittivity of 2.[41] As illustrated in Figure 1a, the cylindrical $TiO_2$ resonators have a diameter of 190 nm and an overall height of 102 nm (of which the cap height is 32 nm, an inherent property of the lift-off method used in fabrication). The designed periodicity in the *x*- and *y*-directions is 408 nm. Figure 1b−g show a stepwise schematic of the fabrication process used to create the tunable dielectric resonator array sample (a detailed description of the synthesis can be found in the Methods). Figure 1h shows a scanning electron micrograph (FEI Verios 460L) of a partial view of the dielectric resonator array.

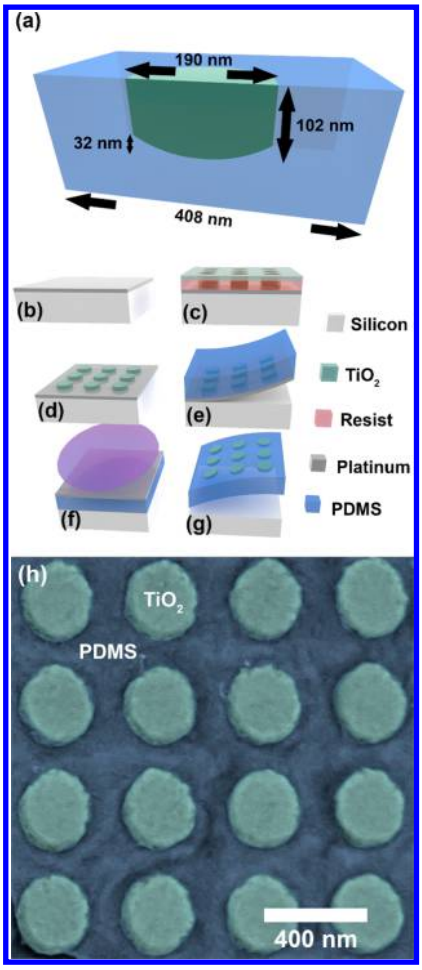


**Figure 1. Dielectric resonator metasurface design and fabrication. (a) Illustration of unit cell geometry, with dimensions for visible wavelength response. (b−g) Nanofabrication process steps: (b) platinum deposition; (c) electron beam lithography for nanopatterning and $TiO_2$ deposition; (d) lift-off removal of $TiO_2$ and resist with subsequent annealing; (e) spin-coating and curing of PDMS with subsequent peel from carrier substrate; (f) schematic of purple plasma plume indicating platinum layer removal by dry etching; and (g) release to create a tunable metasurfaces. (h) $TiO_2$ resonators embedded in PDMS imaged with a scanning electron microscope and represented in false color, where blue indicates PDMS and green $TiO_2$.**

**Optical Characterization of the Metasurfaces.** Transmission measurements are performed with a customized optical spectroscopic system to demonstrate tunability of the metasurface. We measure the transmission spectra of the fabricated sample under mechanical strain, applied uniaxially along the *x*-direction. The measurement schematic is illustrated in Figure 2, with full details provided in the Methods. During measurements, a halogen lamp is used to provide incident white light. In order to introduce mechanical strain, the sample is fixed on a stretching stage with displacement controlled by a graded micrometer screw. To examine polarization dependence of the response, a sheet polarizer controls the excitation polarization along either the *x*-direction (along the direction of applied strain) or the *y*-direction (transverse to applied strain). The transmitted light is collected and measured by a fiber-coupled spectrometer. A bare PDMS substrate under the same amount of stretching is used as a reference.



DOI: 10.1021/acsnano.5b05954
*ACS Nano* 2016, 10, 133−141

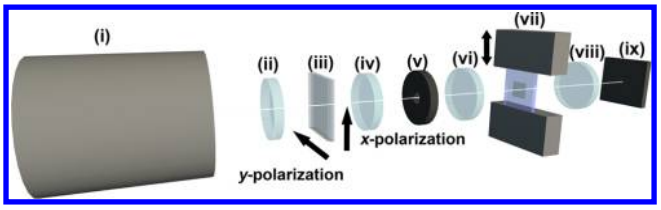


**Figure 2. Schematic of arrangement for optical characterization of dielectric resonator metasurfaces. Components include (i) white light source; (ii) collimating lens; (iii) sheet polarizer; (iv) 40× objective; (v) 50 $\mu$m pinhole; (vi) 20× objective; (vii) tunable dielectric resonator array sample on a stretching stage; (viii) collimating lens; and (ix) fiber-coupled spectrometer.**

**Optical Response of the Unstrained Sample.** We analyze the response of the metasurface first through simulations for the unstrained sample. When excited by normally incident light, the simulated transmission spectrum of the unstrained array exhibits a well-defined electric dipolar mode resonance occurring at 591 nm, as shown in Figure 3a. It is noted that the sharp peak at 582 nm results from a grating effect associated with the infinite array periodicity. The instantaneous field distributions of a cylindrical dielectric resonator associated with this electric dipole mode, represented in Figure 3b,c, show the *E*-field on the $y-z$ plane oscillating in the dielectric resonator center with the *H*-field on the $x-z$ plane circulating around it.

**Mechanically Induced Deformation and Strain.** In order to evaluate the effect of external strain, we have created a three-dimensional (3D) mechanical model to conduct finite-element method (FEM) analysis of the metasurface. Under applied strain, the amount of unit cell displacement depends on the mechanical interplay of the hard high-modulus $TiO_2$ features embedded in the soft low-modulus elastomeric PDMS. To accurately analyze the mechanical deformations in the dielectric resonator array with reasonable computational complexity, we consider a $6 \times 6$ array of unit cells and restrict the area of the PDMS substrate to $10 \times 5$ $\mu m^2$ with a thickness of 2.5 $\mu$m. Details can be found in the Supporting Information.

The PDMS substrate is then subjected to a simulated mechanical deformation with displacement of 0.6 $\mu$m in the *x*-direction, equivalent to 6% strain for the original length of 10 $\mu$m. The resulting total deformation is displayed as a color map in Figure 4a. Despite the presence of the embedded $TiO_2$ features, the result suggests a uniform deformation with no observable distortion of the PDMS substrate in the direction perpendicular to the stretching direction. This response is identical to that of a control substrate without the embedded $TiO_2$ features (see Supporting Information). Figure 4b shows the normalized strain, which is the change in dimension in percentage, occurring in the device. We can observe that the $TiO_2$ disks themselves do not deform under applied strain due to their high modulus, while the soft low-modulus PDMS deforms around them. This mechanical behavior results in a seamless movement of the $TiO_2$ resonators with the substrate. The resulting unit cell period in the direction parallel to the applied strain can therefore be varied consistently across the sample and proportionally to the amount of strain. The associated change in the unit cell period orthogonal to the applied strain can be attributed to the elastomer's intrinsic Poisson's ratio of 0.4[42] and is manifested in the simulation results as an induced compression of the unit cell size in the *y*-direction.

**Tunability of Optical Resonance under Strain.** The observable effect of strain from the mechanical simulation, with specific reference to an alteration of the unit cell periodicity, guides the investigation toward the optical response of the dielectric metasurface. Full-wave electromagnetic simulations are carried out to predict tunability of optical response under strain. The simulation is performed with CST Microwave Studio and employs the unit cell boundary conditions and Floquet excitation ports.[43] The fundamental transverse magnetic (TM) and transverse electric (TE) modes, corresponding respectively to *x*- and *y*-polarized waves, excite the structure in the normal direction. All propagating Floquet modes are observed. The background material is set to PDMS with the nondispersive relative permittivity of 2.[41] In the simulations, the unit cell dimensions are changed in accordance with the FEM mechanical simulation (Figure 4a,b) to imitate the effects of applied strain (stretching) along the *x*-direction together with induced strain (compression) along the *y*-direction.

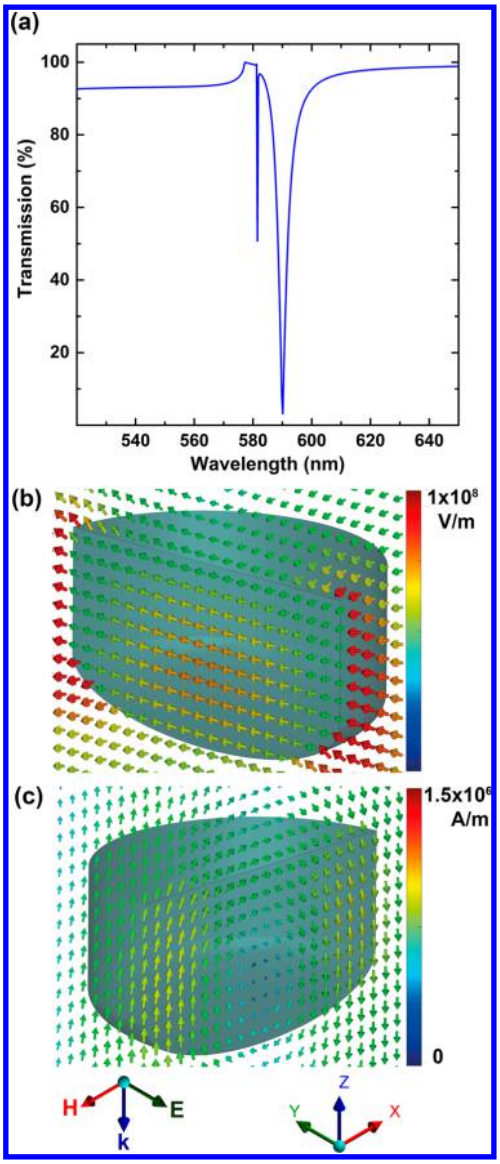


**Figure 3. Resonant electric dipole response of a dielectric resonator in unstrained PDMS matrix. (a) Simulated transmission of the unstrained array sample, for a normally incident wave with *E*-field along the *y*-direction. Simulated (b) *E*-field on the $y-z$ plane and (c) *H*-field on the $x-z$ plane of the resonators in an infinite unstrained array corresponding to the resonance peak in (a).**



DOI: 10.1021/acsnano.5b05954
*ACS Nano* 2016, 10, 133−141

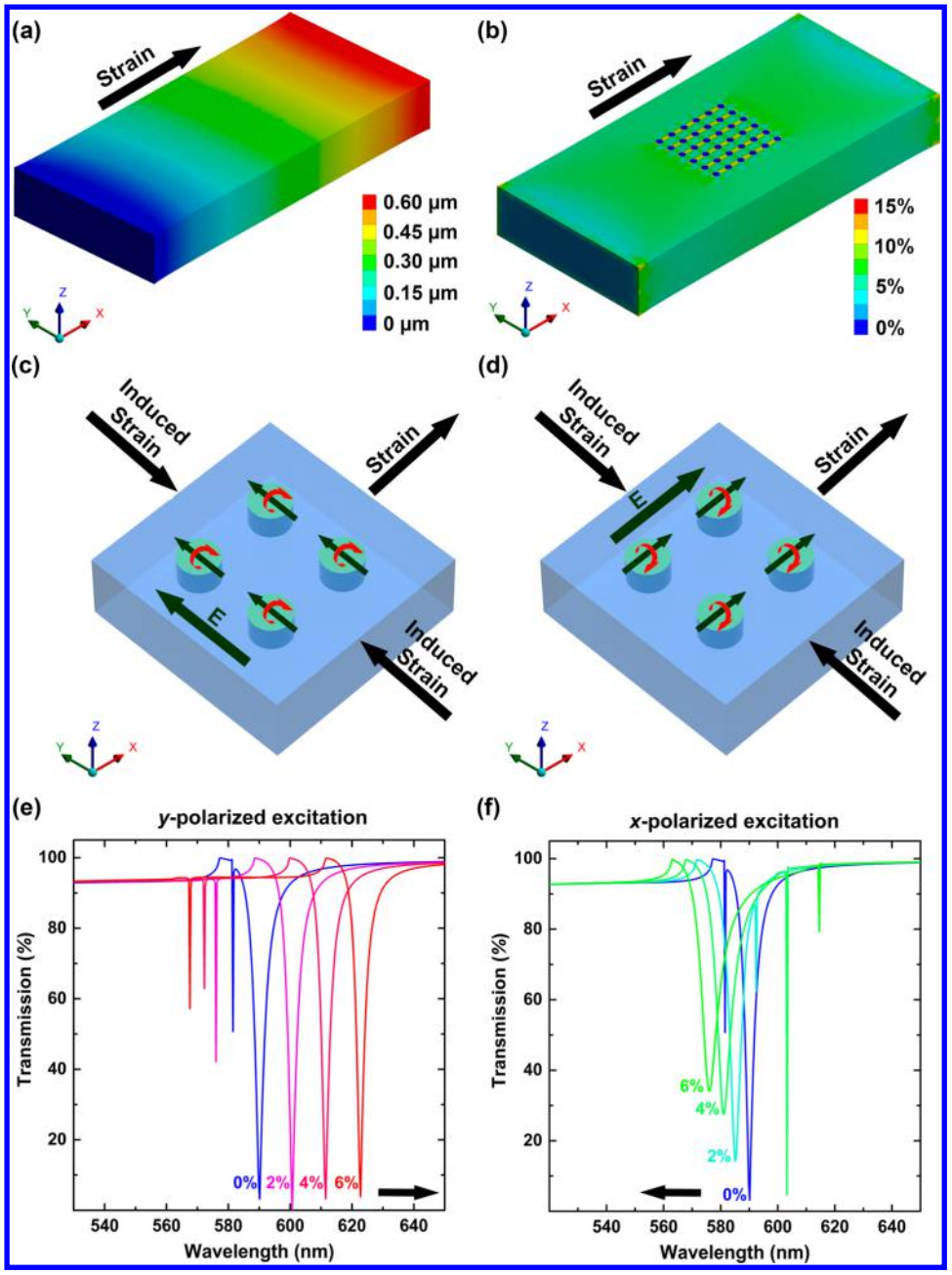


**Figure 4. Mechanical and optical simulations of the metasurface of $TiO_2$ resonators in PDMS.** (a) Total deformation and (b) normalized strain for an applied displacement of 0.6 $\mu$m (6% strain) in the *x*-direction. (c, d) Orientation of the *y*-polarized and *x*-polarized electric dipoles with respect to applied strain. The large dark green arrow denotes the incident *E*-field direction. The modal fields in the cylindrical dielectric resonators are labeled with the green arrows for the *E*-field component (parallel to the excited electric dipoles), while the red arrows indicate the circulating *H*-field component. Simulated resonances under (e) *y*-polarized and (f) *x*-polarized excitation for increasing applied strain, with the black arrow denoting direction of resulting resonance shift.

As illustrated in Figure 4c, for the *y*-polarized incidence, the excited fundamental electric dipoles in the dielectric resonators have the *E*-field transversely coupled and the *H*-field longitudinally coupled along the applied strain direction. For the *x*-polarized incidence in Figure 4d, the converse applies, with the electric dipoles having the *E*-field longitudinally coupled and the *H*-field transversely coupled along the applied strain direction.

Figure 4e,f summarize the simulated transmission spectra of the dielectric resonator array under increasing strain from 0% to 6% for the *y*-polarized and the *x*-polarized incident waves, respectively. In general, the resonance peak undergoes a red-shift under the *y*-polarized excitation, while experiencing a blue-shift under the *x*-polarized excitation. In both figures, the sharp diffraction peak shifts oppositely of the resonance peak, because the incident *E*-field aligns along the unit cell shrinking direction for the *y*-polarization but along the unit cell stretching direction for the *x*-polarization. The red-shift and blue-shift of the dipole resonance imply different dominant effects for transverse and longitudinal mutual coupling among the dielectric resonators. A detailed coupling analysis is presented later by using a Lagrangian model. Here, we emphasize that the resonance shifting is not from the array edge resonance effects,[44] since the array is considered to be 2D-infinite in the simulations.



DOI: 10.1021/acsnano.5b05954
*ACS Nano* 2016, 10, 133−141

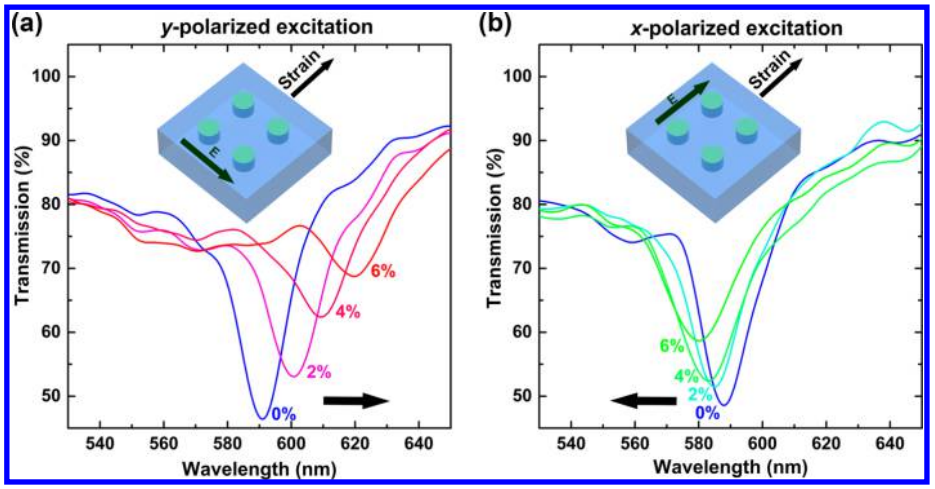


**Figure 5. Polarization-dependent transmission spectra of the metasurfaces with increasing applied strain. (a) *y*-Polarization excitation transverse to applied strain. (b) *x*-Polarization excitation parallel to applied strain.**

The resonance shifting behavior is verified *via* experimental characterization, utilizing nanofabricated samples (Figure 1) and using the test setup in Figure 2. Figure 5a presents the measured results under the *y*-polarized excitation with increasing applied strain. As expected, a clear red-shift of the resonance by 30 nm (5.08%) is observed with the strain increasing from 0% to 6%. The transmission at 591 nm also increases from 47% to 78% as the strain varies from 0% to 6%. Figure 5b presents the measured transmission under the *x*-polarized excitation. In this case, the resonance peak slightly shifts by 6 nm (0.96%) toward the blue and the transmission at 587 nm rises from 48% to 77% when the applied strain increases from 0% to 6%. The contrasting shift toward red and blue is caused by the different transverse and longitudinal coupling strengths, which will be analyzed in greater detail in the next section. The observable resonance arises from the electric dipole mode, since the shifting complies with the simulated electric dipole resonance. Overall, the measured positions of the resonance are in good agreement with simulations. However, the measurement shows a broader resonance line width and gradually increased transmission as the applied strain increases. The resonance broadening and weakening is caused by (i) the divergence angle of the focused beam and (ii) the nonuniformity of the resonator shape, both of which result in slightly different modal field distributions among the resonators. The former cause is corroborated by experimental observations made during system alignment, where it has been found that the resonances are further broadened when using a 50× objective (instead of the 20× objective used in the presented results). Further resonance weakening during stretching is mainly attributed to the increased light leakage from the sample edges. It should be noted that the measured weakening strengths are similar in both *y*- and *x*-polarized excitations, but are obscured by the baseline variation.[45,46]

**Quantitative Analysis of near-Field Interactions among Dielectric Resonators.** In this section, we establish a Lagrangian model to quantitatively investigate the near-field interaction mechanisms among dielectric resonators and interpret the numerical and experimental results. For this symmetrical and uniform dielectric resonator array, the long-distance in-plane interactions are balanced and their impact is significantly less than the near-field interactions.[47] Within the considered optical wavelength range, only the fundamental electric dipolar mode is excited due to the small dimensions and moderate permittivity of the $TiO_2$. Thus, as depicted in Figure 4c, for the *y*-polarized excitation, the *E*-field component of the dielectric resonator fundamental resonant mode is longitudinally coupled in the *y*-direction and transversely coupled in the *x*-direction and *vice versa* for the *H*-field. By increasing the applied strain, it can be then inferred that mainly the *E*-field transverse coupling and the *H*-field longitudinal coupling are altered. On the other hand, under the *x*-polarized excitation, as shown in Figure 4d, mainly the *E*-field longitudinal coupling and the *H*-field transverse coupling are altered with increasing applied strain in the *x*-direction. Both the impacts of the applied strain and the induced strain are incorporated in the Lagrangian analysis. However, the induced strain has a weaker impact on the near-field couplings than the applied strain since the compression due to induced strain is very limited.

To start the analysis, we first consider a single $TiO_2$ dielectric resonator operating in its fundamental electric dipolar mode. It is known that the dielectric resonator operates *via* the displacement current. Therefore, the displacement currents and charges can be described as

**displacement charge density:**

$$\nabla \cdot D \tag{1}$$

**displacement current density:**

$$\frac{\partial D}{\partial t} = \dot{D} \tag{2}$$

where $D$ is the electric flux density and eqs 1 and 2 are linked with the continuity equation for the electric current density. From eqs 1 and 2, the displacement charges and current can therefore be expressed as

**displacement charges:**

$$Q_d = \int_V \nabla \cdot D \, dV \tag{3}$$

**displacement current:**

$$i_d = \oint_S \dot{D} \, dS \tag{4}$$



DOI: 10.1021/acsnano.5b05954
*ACS Nano* 2016, 10, 133−141

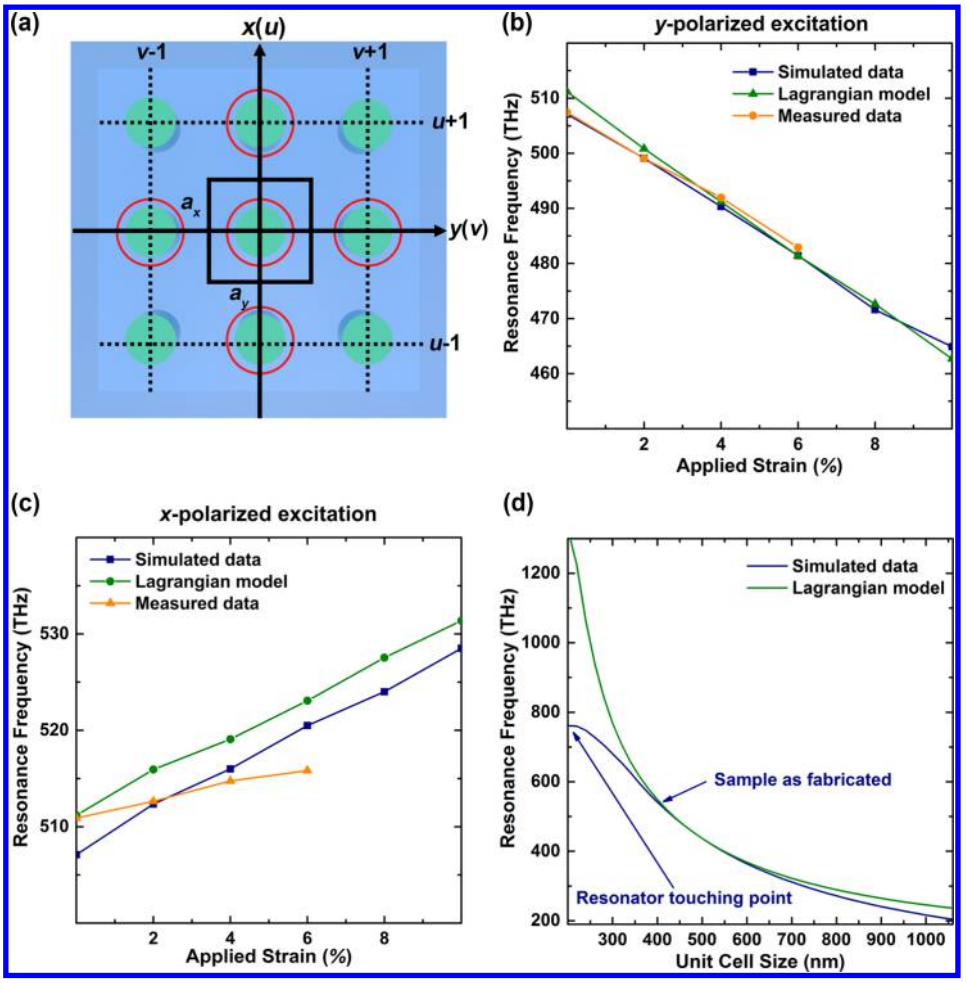


**Figure 6. Lagrangian model fitting to the resonance frequency. The coupling coefficients are as follows: $h_L = 2.10 \times 10^{13}$ nm$^3$, $h_T = 2.50 \times 10^{13}$ nm$^3$, $e_L = 1.40 \times 10^{15}$ nm$^3$, and $e_T = 1.32 \times 10^{16}$ nm$^3$. (a) Illustration of near-field coupling among four neighboring cylindrical $TiO_2$ dielectric resonators. (b) Resonance frequencies when the strain direction is orthogonal to the polarization. (c) Resonance frequencies when the strain direction is parallel to the polarization. (d) Resonance frequencies for square unit cells.**

where $V$ is the volume of the dielectric resonator and $S$ is the area of the resonator cross-section orthogonal to the electric dipole direction. Equations 3 and 4 can be linked with $i_d = dQ_d/dt = \dot{Q}_d$. The Lagrangian model of a single dielectric resonator is thus formulated as[14]

$$\mathcal{L} = \frac{L}{2}\dot{Q}_d^{\,2} - \frac{1}{2C}Q_d^{\,2} \tag{5}$$

where $L$ and $C$ are effective inductance and capacitance of the dielectric resonator. The two terms in eq 5 represent the stored magnetic and electric energy, respectively. Applying the Euler–Lagrangian equation of motion[48]

$$\frac{\partial}{\partial t}\left(\frac{\partial \mathcal{L}}{\partial \dot{Q}_d}\right) = \frac{\partial \mathcal{L}}{\partial Q_d} \tag{6}$$

we arrive at

$$\ddot{Q}_d + Q_d/(LC) = 0 \tag{7}$$

From eq 7, the fundamental electric dipole mode for a single dielectric resonator occurs at the frequency $\omega_0 = 1/(LC)^{1/2}$. For the proposed dielectric resonator design, a value of $\omega_0 = 142.5$ THz is obtained from simulation by using a unit cell size large enough to approximate a resonator in isolation.

In the following, we analyze the effect of the electromagnetic near-field couplings on the electric dipole resonance in the dielectric resonator array. From Figure 6a, the Lagrangian of the coupled resonator system can be expressed as[15]

$$\mathcal{L}_x = \sum_{u,v} \frac{L}{2}[(\ddot{Q}_d)^2_{u,v} - 2\kappa_{HT}(\ddot{Q}_d)_{u,v}(\ddot{Q}_d)_{u+1,v} + 2\kappa_{HL}(\ddot{Q}_d)_{u,v}(\ddot{Q}_d)_{u,v+1}] - \frac{1}{2C}[(Q_d)^2_{u,v} - 2\kappa_{EL}(Q_d)_{u,v}(Q_d)_{u+1,v} + 2\kappa_{ET}(Q_d)_{u,v}(Q_d)_{u,v+1}] \tag{8}$$

Equation 8 describes the electromagnetic near-field interactions under the $x$-polarized excitation. The coupling effects described in eq 8 only take the four nearest neighboring resonators, which are marked with red circles, into consideration, as shown in Figure 6a, and the "+" and "−" signs represent the field attractive and repulsive interactions, respectively. The subscripts for the coupling coefficients $\kappa_{HT}$, $\kappa_{HL}$, $\kappa_{ET}$, and $\kappa_{EL}$ denote the transverse $(T)$ and longitudinal $(L)$ coupling strengths of the magnetic $(h)$ and electric $(e)$ fields. For the $y$-polarized excitation, the transverse and longitudinal coupling coefficients together with their signs in eq 8 should be exchanged. By referring to the near-field expressions for the infinitesimal electric dipole, these coefficients


DOI: 10.1021/acsnano.5b05954
ACS Nano 2016, 10, 133−141

can be linked to the unit cell sizes $a_x$ and $a_y$ as well as the wavenumber $k$ in the PDMS *via*[49]

$$\kappa_{HT} = h_T/(ka_x^3);\ \kappa_{HL} = h_L/(ka_y^3)$$
$$\kappa_{ET} = e_T/a_y^2;\ \kappa_{EL} = e_L/a_x^2 \quad (9)$$

Equation 9 is for the $x$-polarized incidence, and it is noted that $a_x$ and $a_y$ should be exchanged for the $y$-polarized incidence. The constants $h_T$, $h_L$, $e_T$, and $e_L$ represent the effects of an oscillating current source radiating as an electric dipole in the near-field along transverse and longitudinal directions. Applying the Euler–Lagrangian equation in eq 6 to the coupled resonator system in eq 8 yields

$$[(\ddot{Q}_d)_{u,v}^2 - \kappa_{HT}(\ddot{Q}_d)_{u+1,v} + \kappa_{HL}(\ddot{Q}_d)_{u,v+1}] + \frac{1}{LC}[(Q_d)_{u,v}^2 - \kappa_{EL}(Q_d)_{u+1,v} + \kappa_{ET}(Q_d)_{u,v+1}] = 0 \quad (10)$$

Since the plane-wave excitation is uniform across the array, the coupled dielectric resonator array operates in the symmetrical mode. Thus, all the resonators have the same charge distributions, and they oscillate collectively in phase, yielding $(Q_d)_{u,v} = (Q_d)_{u+1,v} = (Q_d)_{u,v+1}$ and $(\ddot{Q}_d)_{u,v} = (\ddot{Q}_d)_{u+1,v} = (\ddot{Q}_d)_{u,v+1}$. Solving eq 10 yields the resonance frequency of the coupled resonator array:

$$\omega_s = \omega_0\sqrt{\frac{1 + \kappa_{ET} - \kappa_{EL}}{1 + \kappa_{HL} - \kappa_{HT}}} \quad (11)$$

where the decoupled resonance frequency $\omega_0$ = 142.5 THz. The unknown constants $h_{T,L}$ and $e_{T,L}$ can be obtained by fitting eq 11 to the simulation and measurement results. From Figure 6b,c, in general, it can be seen that the Lagrangian results in eq 11 fit well the simulated and measured results. A small deviation of the measurement results from the simulation and Lagrangian results is seen in Figure 6c due to an inherent Poisson ratio variation along the $y$-direction,[39] which affects the $x$-polarization results stronger since the dominant transverse coupling is along the $y$-direction. Figure 6d presents the simulated and Lagrangian model results for square unit cells with $a_x = a_y$. The simulated unit cell size ranges from 190 nm, where the resonators touch each other, to 1060 nm. It is seen that the Lagrangian model results have a good agreement with the simulated results for moderate unit cell sizes ranging from 350 to 600 nm. The divergence in the results for smaller unit cells is because the dielectric resonators (dipoles) have a finite size and are not infinitesimally small as assumed in the theoretical model. The limited Lagrangian model accuracy for larger unit cells is mainly because the assumption of near-field interactions in eq 9 is no longer valid.

The coupling coefficients as a function of the unit cell size are plotted in Figure 7 for the case of square unit cells. It is seen that the transverse electric coupling is significantly stronger than the longitudinal electric coupling, while for the magnetic field couplings, the longitudinal and the transverse coupling strengths are similar and relatively weak. Overall, the electric coupling dominates the near-field interactions of dielectric resonators in their electric dipole mode. In effect, the dominant transverse electric coupling results in a clear red-shift when the array is stretched in the direction perpendicular to the polarization. On the other hand, the resonance undergoes a relatively small blue-shift when the strain is applied along the polarization direction. This quantitative finding sheds light on the dominant coupling mechanism and allows further optimization of the dielectric resonator array for maximum tunability.

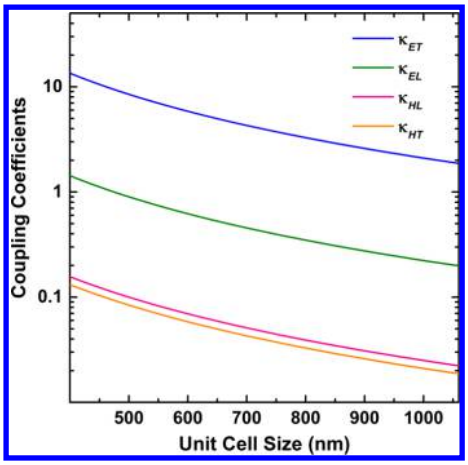


**Figure 7. Influence of metasurface geometry on coupling coefficients. The coupling coefficients (in logarithmic scale) as a function of the square unit cell size (side length).**

## CONCLUSIONS

In this article, we have proposed a mechanically tunable all-dielectric metasurface made of a uniform array of $TiO_2$ cylindrical resonators embedded in an elastomeric PDMS matrix. Subject to the uniaxial strain, the array shows a clear resonance shift toward longer wavelengths for the excitation perpendicular to the strain direction and toward shorter wavelengths for the excitation polarized along the strain direction. With only 6% applied strain, the measured resonance peak shifts 5.08% to red and 0.96% to blue from the base resonance wavelength under different polarizations. This spectral behavior of the $TiO_2$ resonators is well predicted with mechanical and electromagnetic FEM modeling. The Lagrangian model provides an accurate near-field analysis and reveals quantitatively the dominant transverse $E$-field coupling mechanism in the optical dielectric resonator array. This work demonstrates an approach to effectively tune the resonance in all-dielectric low-loss metasurfaces, which suggests a building block for high-efficiency optical devices. The design and analysis provide a fundamental understanding of the coupling mechanism of metasurfaces designed with dielectric resonators and pave the way for next-generation photonic systems.

## METHODS

**Fabrication.** The fabrication of the transparent PDMS-based $TiO_2$ devices relies on the transfer technique described in detail in Gutruf *et al.*[38] The simplified production process is depicted in Figure 1. The process starts with a platinum layer deposited by electron beam evaporation on a standard, cleaned silicon wafer (Figure 1b). A 250 nm thick poly(methyl methacrylate) (PMMA) layer is applied to the platinum-coated silicon wafer *via* spin coating followed by a hard bake at 180 °C. The electron-beam-sensitive PMMA is subsequently exposed using an electron beam lithography system (Nabity EBL system on a FEI Nova SEM equipped with a field emission gun) by writing the negative mask of the dielectric resonator array in a serial process. The written structures are 190 nm diameter holes with a separation of 420 nm in both the $x$- and $y$-directions. The dielectric resonator array consists of 280 × 280 periods, giving it a total dimension of 118 × 118 $\mu m^2$. A subsequent immersion in a MIBK developer is used to wash away the regions exposed to the electron beam. The $TiO_2$ dielectric layer of 102 nm thickness is then deposited by electron beam evaporation (Figure 1c). Subsequently, lift-off is performed in an acetone bath to remove the excess $TiO_2$ (Figure 1d). The lift-off is followed by an


DOI: 10.1021/acsnano.5b05954
*ACS Nano* 2016, 10, 133–141

annealing step of 600 °C for 2 h under vacuum[27] to synthesize the anatase phase of $TiO_2$ to ensure low loss. This is followed by the removal of the $TiO_2$/Pt sandwich from its rigid carrier by casting PDMS (2 mm thick) onto the $TiO_2$ layer, with a subsequent hot plate cure at 120 °C for 8 min and an immediate peel-off (Figure 1e). It is significant to note that the step depicted in Figure 1e results in a shrinkage of the PDMS substrate on release from the substrate, due to compressive strain introduced by curing the PDMS at an elevated temperature (120 °C). This decrease in volume results in a multiaxial compression of ∼2.9%. This phenomenon has been well characterized and accounted for in our work by ensuring the nanofabrication pattern with unit cell dimensions that are larger (420 nm, in comparison to the 408 nm defined by the design). The wafer-sized $TiO_2$/PDMS device is flipped over onto a silicon carrier and the Pt layer removed by reactive ion etching (7.5 min, 100 W, Ar atmosphere, 70 mTorr working pressure), leaving the dielectric cylinders exposed (Figure 1f). The device is then carefully lifted off the carrier and diced into 50 mm × 50 mm specimens for measurements (Figure 1g).

**Characterization.** A schematic of the optical characterization setup is shown in Figure 2, with the components denoted by (i) to (ix) in the figure described below.

A 20 W BWTEK BIP 2.0 tungsten halogen lamp (i) is selected as the white light source. To obtain sufficient incident power, the integration housing sphere is removed so that the lamp illuminates forward directly in a broad angle. A two-inch diameter, 60 mm focal length biconvex lens and a one-inch diameter, 25.4 mm focal length plano-convex lens (ii) are used to collect and collimate the broadly diverged light into a 40 × 0.65 numerical aperture objective (iv). A Newport 5511 sheet polarizer (iii) on a rotating mount is positioned right before the 40× objective for polarization selection. Several black paper cards and an aluminum light housing box are utilized to prevent randomly scattered light. The 40× objective focuses the light beam into a 50 $\mu$m pinhole (v). The measured power of the light from the pinhole is 82 $\mu$W, ensuring sufficient signal power over the noise level. An Olympus RMS20X 20× 0.4 numerical aperture achromatic objective (vi) is used to focus the light down to ∼140 $\mu$m to excite the dielectric resonator array sample in its center. The selection of the 20× objective takes both the beam divergence angle and focused beam size into consideration. The sample is mounted on a stretching stage (vii) with a minimum stretching step of 10 $\mu$m. The transmitted light is collimated by a one-inch diameter, 30 mm focal length plano-convex lens (viii) into an SMA905 fiber coupler connected with a BWTEK FPC 600 $\mu$m core optical fiber. The fiber guides the transmitted light into the BRC115P Exemplar CCD spectrometer (ix) for measurement. During the measurements, a CS01-200 digital microscope is used for observing the sample and for focusing the incident beam onto the center of the dielectric resonator array. The sample is measured under 0, 2%, 4%, and 6% strain applied along the $x$-direction with both the $x$- and $y$-polarized incident waves.

## ASSOCIATED CONTENT

### Supporting Information

The Supporting Information is available free of charge on the ACS Publications website at DOI: 10.1021/acsnano.5b05954.

Summary of mechanical simulation details (PDF)

## AUTHOR INFORMATION


### Corresponding Author

*E-mail: christophe.fumeaux@adelaide.edu.au.

### Author Contributions

#P. Gutruf and C. Zou contributed equally.


### Notes

The authors declare no competing financial interest.

## ACKNOWLEDGMENTS

P.G. acknowledges an Australian Government Endeavour International Postgraduate Research Scholarship. M.B. acknowledges an Australian Research Council early career fellowship (DE160100023). C.F. acknowledges the Australian Research Council Future Fellowship funding scheme (FT100100585). The authors acknowledge the facilities and technical assistance of the Australian Microscopy and Microanalysis Research Facility at the RMIT Microscopy and Microanalysis Facility at RMIT University.

## REFERENCES


(1) Yu, N.; Capasso, F. Flat Optics with Designer Metasurfaces. *Nat. Mater.* **2014**, *13*, 139−150.

(2) Kildishev, A. V.; Boltasseva, A.; Shalaev, V. M. Planar Photonics with Metasurfaces. *Science* **2013**, *339*, 1232009.

(3) Yu, N.; Genevet, P.; Kats, M. A.; Aieta, F.; Tetienne, J.-P.; Capasso, F.; Gaburro, Z. Light Propagation with Phase Discontinuities: Generalized Laws of Reflection and Refraction. *Science* **2011**, *334*, 333−337.

(4) Sun, S.; Yang, K.-Y.; Wang, C.-M.; Juan, T.-K.; Chen, W. T.; Liao, C. Y.; He, Q.; Xiao, S.; Kung, W.-T.; Guo, G.-Y. High-Efficiency Broadband Anomalous Reflection by Gradient Meta-surfaces. *Nano Lett.* **2012**, *12*, 6223−6229.

(5) Li, Z.; Palacios, E.; Butun, S.; Aydin, K. Visible-Frequency Metasurfaces for Broadband Anomalous Reflection and High-Efficiency Spectrum Splitting. *Nano Lett.* **2015**, *15*, 1615−1621.

(6) Yang, Y.; Wang, W.; Moitra, P.; Kravchenko, I. I.; Briggs, D. P.; Valentine, J. Dielectric Meta-Reflectarray for Broadband Linear Polarization Conversion and Optical Vortex Generation. *Nano Lett.* **2014**, *14*, 1394−1399.

(7) Huang, L.; Chen, X.; Mühlenbernd, H.; Zhang, H.; Chen, S.; Bai, B.; Tan, Q.; Jin, G.; Cheah, K.-W.; Qiu, C.-W.; et al. Three-Dimensional Optical Holography Using a Plasmonic Metasurface. *Nat. Commun.* **2013**, *4*, 2808.

(8) Wu, M. C.; Solgaard, O.; Ford, J. E. Optical MEMS for Lightwave Communication. *J. Lightwave Technol.* **2006**, *24*, 4433−4454.

(9) Zheludev, N. I.; Kivshar, Y. S. From Metamaterials to Metadevices. *Nat. Mater.* **2012**, *11*, 917−924.

(10) Prodan, E.; Radloff, C.; Halas, N. J.; Nordlander, P. A Hybridization Model For the Plasmon Response of Complex Nanostructures. *Science* **2003**, *302*, 419−422.

(11) Liu, N.; Liu, H.; Zhu, S.; Giessen, H. Stereometamaterials. *Nat. Photonics* **2009**, *3*, 157−162.

(12) Powell, D. A.; Hannam, K.; Shadrivov, I. V.; Kivshar, Y. S. Near-field Interaction of Twisted Split-Ring Resonators. *Phys. Rev. B: Condens. Matter Mater. Phys.* **2011**, *83*, 235420.

(13) Meinzer, N.; Barnes, W. L.; Hooper, I. R. Plasmonic Meta-Atoms and Metasurfaces. *Nat. Photonics* **2014**, *8*, 889−898.

(14) Powell, D. A.; Lapine, M.; Gorkunov, M. V.; Shadrivov, I. V.; Kivshar, Y. S. Metamaterial Tuning by Manipulation of Near-Field Interaction. *Phys. Rev. B: Condens. Matter Mater. Phys.* **2010**, *82*, 155128.

(15) Withayachumnankul, W.; Fumeaux, C.; Abbott, D. Near-Field Interactions in Electric Inductive−Capacitive Resonators for Metamaterials. *J. Phys. D: Appl. Phys.* **2012**, *45*, 485101.

(16) Sersic, I.; Frimmer, M.; Verhagen, E.; Koenderink, A. F. Electric and Magnetic Dipole Coupling in Near-Infrared Split-Ring Metamaterial Arrays. *Phys. Rev. Lett.* **2009**, *103*, 213902.

(17) Li, J.; Shah, C. M.; Withayachumnankul, W.; Ung, B. S.-Y.; Mitchell, A.; Sriram, S.; Bhaskaran, M.; Chang, S.; Abbott, D. Mechanically Tunable Terahertz Metamaterials. *Appl. Phys. Lett.* **2013**, *102*, 121101.

(18) Driscoll, T.; Palit, S.; Qazilbash, M. M.; Brehm, M.; Keilmann, F.; Chae, B.-G.; Yun, S.-J.; Kim, H.-T.; Cho, S.; Jokerst, N. M. Dynamic Tuning of an Infrared Hybrid-Metamaterial Resonance using Vanadium Dioxide. *Appl. Phys. Lett.* **2008**, *93*, 024101.

(19) Seo, M.; Kyoung, J.; Park, H.; Koo, S.; Kim, H.-S.; Bernien, H.; Kim, B. J.; Choe, J. H.; Ahn, Y. H.; Kim, H.-T. Active Terahertz Nanoantennas Based on $VO_2$ phase transition. *Nano Lett.* **2010**, *10*, 2064−2068.




DOI: 10.1021/acsnano.5b05954
*ACS Nano* 2016, 10, 133−141

(20) Benz, A.; Montaño, I.; Klem, J. F.; Brener, I. Tunable Metamaterials Based on Voltage Controlled Strong Coupling. *Appl. Phys. Lett.* **2013**, *103*, 263116.
(21) Ou, J.-Y.; Plum, E.; Jiang, L.; Zheludev, N. I. Reconfigurable Photonic Metamaterials. *Nano Lett.* **2011**, *11*, 2142−2144.
(22) Pryce, I. M.; Aydin, K.; Kelaita, Y. A.; Briggs, R. M.; Atwater, H. A. Highly Strained Compliant Optical Metamaterials With Large Frequency Tunability. *Nano Lett.* **2010**, *10*, 4222−4227.
(23) Aksu, S.; Huang, M.; Artar, A.; Yanik, A. A.; Selvarasah, S.; Dokmeci, M. R.; Altug, H. Flexible plasmonics on unconventional and nonplanar substrates. *Adv. Mater.* **2011**, *23*, 4422−4430.
(24) Millyard, M. G.; Huang, F. M.; White, R.; Spigone, E.; Kivioja, J.; Baumberg, J. J. Stretch-Induced Plasmonic Anisotropy of Self-Assembled Gold Nanoparticle Mats. *Appl. Phys. Lett.* **2012**, *100*, 073101.
(25) Boardman, A. D.; Grimalsky, V. V.; Kivshar, Y. S.; Koshevaya, S. V.; Lapine, M.; Litchinitser, N. M.; Malnev, V. N.; Noginov, M.; Rapoport, Y. G.; Shalaev, V. M. Active and Tunable Metamaterials. *Laser Photonics Rev.* **2011**, *5*, 287−307.
(26) Poutrina, E.; Huang, D.; Smith, D. R. Analysis of nonlinear electromagnetic metamaterials. *New J. Phys.* **2010**, *12*, 093010.
(27) Zou, L.; Withayachumnankul, W.; Shah, C. M.; Mitchell, A.; Bhaskaran, M.; Sriram, S.; Fumeaux, C. Dielectric Resonator Nanoantennas at Visible Frequencies. *Opt. Express* **2013**, *21*, 1344−1352.
(28) Filonov, D. S.; Krasnok, A. E.; Slobozhanyuk, A. P.; Kapitanova, P. V.; Nenasheva, E. A.; Kivshar, Y. S.; Belov, P. A. Experimental Verification of the Concept of All-Dielectric Nanoantennas. *Appl. Phys. Lett.* **2012**, *100*, 201113.
(29) Staude, I.; Miroshnichenko, A. E.; Decker, M.; Fofang, N. T.; Liu, S.; Gonzales, E.; Dominguez, J.; Luk, T. S.; Neshev, D. N.; Brener, I. Tailoring Directional Scattering Through Magnetic and Electric Resonances in Subwavelength Silicon Nanodisks. *ACS Nano* **2013**, *7*, 7824−7832.
(30) Krasnok, A. E.; Miroshnichenko, A. E.; Belov, P. A.; Kivshar, Y. S. All-Dielectric Optical Nanoantennas. *Opt. Express* **2012**, *20*, 20599−20604.
(31) Decker, M.; Staude, I.; Falkner, M.; Dominguez, J.; Neshev, D. N.; Brener, I.; Pertsch, T.; Kivshar, Y. S. High-Efficiency Dielectric Huygens' Surfaces. *Adv. Opt. Mater.* **2015**, *3*, 813−820.
(32) Zou, L.; Withayachumnankul, W.; Shah, C. M.; Mitchell, A.; Klemm, M.; Bhaskaran, M.; Sriram, S.; Fumeaux, C. Efficiency and Scalability of Dielectric Resonator Antennas at Optical Frequencies. *IEEE Photonics J.* **2014**, *6*, 1−10.
(33) Zou, L.; López-García, M.; Withayachumnankul, W.; Shah, C. M.; Mitchell, A.; Bhaskaran, M.; Sriram, S.; Oulton, R.; Klemm, M.; Fumeaux, C. Spectral and Angular Characteristics of Dielectric Resonator Metasurface at Optical Frequencies. *Appl. Phys. Lett.* **2014**, *105*, 191109.
(34) Zou, C.; Withayachumnankul, W.; Shadrivov, I. V.; Kivshar, Y. S.; Fumeaux, C. Directional Excitation of Surface Plasmons by Dielectric Resonators. *Phys. Rev. B: Condens. Matter Mater. Phys.* **2015**, *91*, 085433.
(35) Van de Groep, J.; Polman, A. Designing Dielectric Resonators on Substrates: Combining Magnetic and Electric Resonances. *Opt. Express* **2013**, *21*, 26285−26302.
(36) Sautter, J.; Staude, I.; Decker, M.; Rusak, E.; Neshev, D. N.; Brener, I.; Kivshar, Y. S. Active Tuning of All-Dielectric Metasurfaces. *ACS Nano* **2015**, *9*, 4308−4315.
(37) Seghir, R.; Arscott, S. Mechanically Robust, Electrically Stable Metal Arrays on Plasma-oxidized Polydimethylsiloxane for Stretchable Technologies. *J. Appl. Phys.* **2015**, *118*, 045309.
(38) Gutruf, P.; Shah, C. M.; Walia, S.; Nili, H.; Zoolfakar, A. S.; Karnutsch, C.; Kalantar-zadeh, K.; Sriram, S.; Bhaskaran, M. Transparent Functional Oxide Stretchable Electronics: Micro-Tectonics Enabled High Strain Electrodes. *NPG Asia Mater.* **2013**, *5*, e62.
(39) Gutruf, P.; Zeller, E.; Walia, S.; Nili, H.; Sriram, S.; Bhaskaran, M. Stretchable and Tunable Microtectonic ZnO-Based Sensors and Photonics. *Small* **2015**, *11*, 4532−4539.
(40) Zhu, L.; Kapraun, J.; Ferrara, J.; Chang-Hasnain, C. J. Flexible Photonic Metastructures for Tunable Coloration. *Optica* **2015**, *2*, 255−258.
(41) Mark, J. E. *Polymer Data Handbook*; Oxford University Press: New York, 1999.
(42) Xia, Y.; Kim, E.; Zhao, X.-M.; Rogers, J. A.; Prentiss, M.; Whitesides, G. M. Complex Optical Surfaces Formed by Replica Molding Against Elastomeric Masters. *Science* **1996**, *273*, 347−349.
(43) Mias, C.; Webb, J.; Ferrari, R. Finite Element Modelling of Electromagnetic Waves in Doubly and Triply Periodic Structures. *IEE Proc.: Optoelectron.* **1999**, *146*, 111−118.
(44) Tucker, E.; D'Archangel, J.; Raschke, M. B.; Boreman, G. Near-Field Investigation of the Effect of the Array Edge on the Resonance of Loop Frequency Selective Surface Elements at Mid-Infrared Wavelengths. *Opt. Express* **2015**, *23*, 10974−10985.
(45) Sekiya, T.; Yagisawa, T.; Kamiya, N.; Das Mulmi, D.; Kurita, S.; Murakami, Y.; Kodaira, T. Defects in anatase $TiO_2$ single crystal controlled by heat treatments. *J. Phys. Soc. Jpn.* **2004**, *73*, 703−710.
(46) Kuznetsov, V. N.; Serpone, N. On the origin of the spectral bands in the visible absorption spectra of visible-light-active $TiO_2$ specimens analysis and assignments. *J. Phys. Chem. C* **2009**, *113*, 15110−15123.
(47) Khunsin, W.; Brian, B.; Dorfmüller, J.; Esslinger, M.; Vogelgesang, R.; Etrich, C.; Rockstuhl, C.; Dmitriev, A.; Kern, K. Long-Distance Indirect Excitation of Nanoplasmonic Resonances. *Nano Lett.* **2011**, *11*, 2765−2769.
(48) Morin, D. *Introduction to Classical Mechanics: with Problems and Solutions*; Cambridge University Press, 2008.
(49) Balanis, C. A. *Antenna Theory: Analysis and Design*; John Wiley & Sons, 2012.


DOI: 10.1021/acsnano.5b05954
*ACS Nano* 2016, 10, 133−141